# Approaching faithful templates for nonspinning binary black holes using the effective-one-body approach

Alessandra Buonanno,[1] Yi Pan,[1] John G. Baker,[2] Joan Centrella,[2] Bernard J. Kelly,[2]
Sean T. McWilliams,[3] and James R. van Meter[2,4]

[1]*Maryland Center for Fundamental Physics, Department of Physics, University of Maryland, College Park, Maryland 20742, USA*
[2]*Gravitational Astrophysics Laboratory, NASA Goddard Space Flight Center, 8800 Greenbelt Road, Greenbelt, Maryland 20771, USA*
[3]*Department of Physics, University of Maryland, College Park, Maryland 20742, USA*
[4]*Center for Space Science and Technology, Physics Department, University of Maryland Baltimore County, 1000 Hilltop Circle,
Baltimore, Maryland 21250, USA*

We present an accurate approximation of the full gravitational radiation waveforms generated in the merger of noneccentric systems of two nonspinning black holes. Utilizing information from recent numerical relativity simulations and the natural flexibility of the effective-one-body (EOB) model, we extend the latter so that it can successfully match the numerical relativity waveforms during the last stages of inspiral, merger, and ringdown. By ''successfully'' here, we mean with phase differences $\lesssim 8\%$ of a gravitational-wave cycle accumulated by the end of the ringdown phase, maximizing only over time of arrival and initial phase. We obtain this result by simply adding a 4-post-Newtonian order correction in the EOB radial potential and determining the (constant) coefficient by imposing high-matching performances with numerical waveforms of mass ratios $m_1/m_2 = 1, 3/2, 2$ and $4$, $m_1$ and $m_2$ being the individual black-hole masses. The final black-hole mass and spin predicted by the numerical simulations are used to determine the ringdown frequency and decay time of three quasinormal-mode damped sinusoids that are attached to the EOB inspiral-(plunge) waveform at the EOB light ring. The EOB waveforms might be tested and further improved in the future by comparison with extremely long and accurate inspiral numerical relativity waveforms. They may be already employed for coherent searches and parameter estimation of gravitational waves emitted by nonspinning coalescing binary black holes with ground-based laser-interferometer detectors.

PACS numbers: 04.25.Nx, 04.25.Dm, 04.30.Db, 04.70.Bw

## I. INTRODUCTION

The network of ground-based laser-interferometer gravitational-wave (GW) detectors, such as LIGO [1], VIRGO [2], GEO [3], and TAMA [4], are currently operating at design sensitivity (except for VIRGO which is expected to reach design sensitivity within 1 yr) and are searching for GWs in the frequency range of $10$–$10^3$ Hz. Within the next decade these detectors will likely be complemented by the laser-interferometer space antenna (LISA) [5], a joint venture between NASA and ESA, which will search for GWs in the frequency range $3 \times 10^{-5}$–$10^{-1}$ Hz.

Binary systems composed of black holes (BHs) and/or neutron stars (NSs) are among the most promising sources. The search for GWs from coalescing binary systems and the extraction of parameters are based on the matched-filtering technique [6], which requires accurate knowledge of the waveform of the incoming signal. Recent comparisons [7–13] between numerical and post-Newtonian (PN) analytic waveforms emitted by nonspinning binary BH systems suggest that it should be possible to design purely analytic templates with the full numerics used to guide the patching together of the inspiral and ringdown (RD) waveforms. This is an important avenue to template construction as eventually thousands of waveform templates may

be needed to extract the GW signal from the noise, an impossible demand for numerical relativity (NR) alone.

The best-developed *analytic* method for describing the two-body dynamics of comparable-mass BHs and predicting the GW signal is undoubtedly the PN method [14], which for compact bodies is essentially an expansion in the characteristic orbital velocity $v/c$. Template predictions are currently available through 3.5PN order ($v^7/c^7$) [15–18], if the compact objects do not carry spin, and 2.5PN order ($v^5/c^5$) [19] if they carry spin. Resummation of the PN expansion aimed at pushing analytic calculations until the final stage of evolution, including the transition inspiral-merger-ringdown, have been proposed. In 1999, the authors of Ref. [20] introduced a nonperturbative resummation of the two-body conservative dynamics, the so-called effective-one-body (EOB) approach [20]. The original EOB model was computed using the 2PN conservative dynamics. It was then extended to 3PN order [21] when the 3PN calculation was completed [18] and then to spinning BHs [22]. The EOB approach has been the *only* analytic approach able to predict, within $\sim 10\%$ of accuracy, the spin of the final BH [23]. Recently, by combining the EOB approach with test-mass limit predictions for the energy released during the merger-ringdown phases, Ref. [24] has refined this prediction obtaining $\sim 2\%$ of accuracy. The EOB approach also provided a complete waveform, from

inspiral to ringdown, for nonspinning [23,25] and spinning, precessing binary systems [26]. To include accurately the radiation-reaction contribution, the EOB approach uses the Padé resummation of the GW flux, as proposed in Ref. [27].

By construction the EOB approach recovers exactly geodesic motion in the test-mass limit. In the comparable-mass limit the EOB approach provides a non-perturbative resummation of the dynamics which today can be tested and improved by comparing it to NR results. NR simulations are in fact the best tool to describe the non-linear, strong-gravity regime of comparable-mass binary coalescences. As we shall see below, because of the reduction of the dynamics to *a few* crucial functions determining the inspiral evolution [20,22,23], and because of the rather simple procedure to match the inspiral(-plunge) waveform to the ringdown waveform, the EOB model is particularly suitable for fitting to the numerical results [28,29]. In this paper we shall employ its flexibility [22,30,31] to obtain accurate waveforms for potentially the full range of non-spinning binary BHs. We shall test the analytic waveforms against the numerical ones for mass ratios ranging between $m_1/m_2 = 1$ and $m_1/m_2 = 4$, with $m_1$ and $m_2$ being the BH masses. The method also allows us to predict the wave-forms for mass ratios $m_1/m_2 > 4$. These waveforms will be tested against numerical results when accurate long numerical simulations for mass ratios $m_1/m_2 > 4$ become available. In this paper the comparisons are carried out using simulations from the NASA-Goddard group.

The paper is organized as follows. In Sec. II we briefly review the EOB model. In Sec. III we *improve* the EOB model by adding a 4PN order unknown coefficient to the two-body conservative dynamics. In Sec. IV we complete the EOB model using inputs from NR simulations. In Sec. V we compare the improved EOB model to two accurate, long numerical simulations with mass ratios 1:1 and 4:1, determine the best-fit 4PN order coefficient, and discuss the matching performances for several dominant modes. Section VI summarizes our main conclusions. The Appendix refers to shorter numerical simulations with mass ratios 2:1 and 3:2.

## II. EFFECTIVE-ONE-BODY MODEL FOR NONSPINNING BLACK HOLE BINARIES

At the end of the 1990s, in the absence of NR results and with the urgent need of providing templates to search for comparable-mass BHs, some resummation techniques of the post-Newtonian series were proposed. The general philosophy underlying these techniques [20,27] was to first *resum* in the test-mass−limit case the two crucial ingredients determining the gravitational-wave signal: the two-body energy and the gravitational-wave energy flux. In fact, in the test-mass−limit case these ingredients are known exactly. Secondly, it was assumed that the re-summed quantities will *also* be a good representation of the comparable-mass case, viewed as a smooth deformation of the test-mass−limit case.

The resummation technique discussed in this section, the EOB approach [20], was originally inspired by a simi-lar approach introduced by Brézin, Itzykson, and Zinn-Justin [32] to study two electromagnetically interacting particles with comparable masses. The basic idea of the EOB approach is to map the *real* conservative two-body dynamics up to the highest PN order available, onto an *effective* one-body problem, where a test particle of mass $\mu = m_1 m_2/M$, with $m_1$, $m_2$ the BH masses and $M = m_1 + m_2$, moves in some effective background metric $g_{\mu\nu}^{\text{eff}}$. This mapping has been worked out within the Hamilton-Jacobi formalism, by requiring that while the action variables of the real and effective description coin-cide (i.e., $L_{\text{real}} = L_{\text{eff}}$, $\mathcal{I}_{\text{real}} = \mathcal{I}_{\text{eff}}$, where $L$ denotes the total angular momentum, and $\mathcal{I}$ the radial action variable), the energy axis is allowed to change: $E_{\text{real}} = f(E_{\text{eff}})$, where $f$ is a generic function determined by the mapping. By applying the above rules defining the mapping, it was found [20] in the nonspinning case that as long as radiation-reaction effects are not taken into account, the effective metric is just a deformation of the Schwarzschild metric, with deformation parameter $\eta = \mu/M$.

The explicit expression of the nonspinning EOB effec-tive Hamiltonian through 3PN order is [20,21]:

$$H_{\text{eff}}(\mathbf{r}, \boldsymbol{p}) = \mu \hat{H}_{\text{eff}}(\mathbf{r}, \boldsymbol{p}) = \mu \sqrt{A(r)[1 + \mathbf{p}^2 + (\frac{A(r)}{D(r)} - 1)(\mathbf{n} \cdot \mathbf{p})^2 + \frac{1}{r^2}(z_1(\mathbf{p}^2)^2 + z_2 \mathbf{p}^2(\mathbf{n} \cdot \mathbf{p})^2 + z_3(\mathbf{n} \cdot \mathbf{p})^4)]}, \quad (1)$$

with $\mathbf{r}$ and $\boldsymbol{p}$ being the reduced dimensionless variables; $\mathbf{n} = \mathbf{r}/r$ where we set $r = |\mathbf{r}|$. In the absence of spins the motion is constrained to a plane. Introducing polar coor-dinates $(r, \varphi, p_r, p_\varphi)$, the EOB effective metric reads

$$ds_{\text{eff}}^2 \equiv g_{\mu\nu}^{\text{eff}} dx^\mu dx^\nu$$

$$= -A(r)c^2 dt^2 + \frac{D(r)}{A(r)} dr^2 + r^2(d\theta^2 + \sin^2\theta d\varphi^2). \quad (2)$$

The EOB real Hamiltonian is

$$H_{\text{real}} = M\sqrt{1 + 2\eta\left(\frac{H_{\text{eff}} - \mu}{\mu}\right)} - M, \quad (3)$$

and we define $\hat{H}_{\text{real}} = H_{\text{real}}/\mu$. Remarkably, as originally observed in Ref. [20], the mapping between the real and the effective Hamiltonians given by Eq. (3) coincides with the mapping obtained in the context of quantum electro-dynamics in Ref. [32], where the authors mapped the one-

body relativistic Balmer formula onto the two-body energy formula. Moreover, Eq. (3) holds at 2PN and 3PN order [21]. The coefficients $z_1$, $z_2$, and $z_3$ in Eq. (1) are arbitrary, subject to the constraint

$$8z_1 + 4z_2 + 3z_3 = 6(4 - 3\eta)\eta. \qquad (4)$$

The coefficients $A(r)$ and $D(r)$ in Eq. (1) have been calculated through 3PN order [20,21]. In Taylor-expanded form they read:

$$A_T^{3PN}(r) = 1 - \frac{2}{r} + \frac{2\eta}{r^3} + \left[ \left( \frac{94}{3} - \frac{41}{32}\pi^2 \right)\eta - z_1 \right]\frac{1}{r^4}, \qquad (5)$$

$$D_T^{3PN}(r) = 1 - \frac{6\eta}{r^2} + [7z_1 + z_2 + 2\eta(3\eta - 26)]\frac{1}{r^3}. \quad (6)$$

at 3PN order where

$$a_4(\eta, z_1) = \left[ \left( \frac{94}{3} - \frac{41}{32}\pi^2 \right)\eta - z_1 \right]. \qquad (9)$$

For the coefficient $D(r)$ at 3PN order we use the Padé approximant

$$D_{P_3^0}^{3PN}(r) = \frac{r^3}{r^3 + 6\eta r + 2\eta(26 - 3\eta)}. \qquad (10)$$

To include radiation-reaction effects we write the EOB Hamilton equations in terms of the reduced quantities $\hat{H}$, $\hat{t} = t/M$, $\hat{\omega} = \omega M$ [23], as[1]

$$\frac{dr}{d\hat{t}} = \frac{\partial \hat{H}}{\partial p_r}(r, p_r, p_\varphi), \qquad (11)$$

$$\frac{d\varphi}{d\hat{t}} \equiv \hat{\omega} = \frac{\partial \hat{H}}{\partial p_\varphi}(r, p_r, p_\varphi), \qquad (12)$$

In principle we could explore the possibility of determining some of the $z_i$ coefficients through a fit with the numerical results. However, here we do not follow this possibility and, as in previous works, except for Refs. [31,33], we set $z_1 = z_2 = 0$, $z_3 = 2(4 - 3\eta)\eta$. The EOB effective potential $A_T^{3PN}(r)$ does not lead to a last-stable circular orbit (LSO), contrary to what happens in the 2PN-accurate case [20]. This is due to the rather large value of the 3PN coefficient $94/3 - 41/32\pi^2 \simeq 18.688$ entering the PN expansion of $A(r)$. Replacing the PN-expanded form of $A(r)$ by a Padé approximant cures this problem [21]. The Padé approximant is

$$A_{P_2^1}^{2PN}(r) = \frac{r(-4 + 2r + \eta)}{2r^2 + 2\eta + r\eta}, \qquad (7)$$

at 2PN order and

$$A_{P_3^1}^{3PN}(r) = \frac{r^2[(a_4(\eta, 0) + 8\eta - 16) + r(8 - 2\eta)]}{r^3(8 - 2\eta) + r^2[a_4(\eta, 0) + 4\eta] + r[2a_4(\eta, 0) + 8\eta] + 4[\eta^2 + a_4(\eta, 0)]}, \qquad (8)$$

$$\frac{dp_r}{d\hat{t}} = -\frac{\partial \hat{H}}{\partial r}(r, p_r, p_\varphi), \qquad (13)$$

$$\frac{dp_\varphi}{d\hat{t}} = \hat{F}^\varphi[\hat{\omega}(r, p_r, p_\varphi)], \qquad (14)$$

where for the $\varphi$ component of the radiation-reaction force we shall use the $P$ approximant [23,27]

$$\hat{F}^\varphi_{P_N} \equiv -\frac{1}{\eta v_\omega^3}\mathcal{F}_{P_N}[v_\omega] = -\frac{32}{5}\eta v_\omega^7 \frac{f_{P_N}(v_\omega; \eta)}{1 - v_\omega/v_{\text{pole}}(\eta)}, \qquad (15)$$

where $v_\omega \equiv \hat{\omega}^{1/3} \equiv (d\varphi/d\hat{t})^{1/3}$. The coefficients $f_{P_N}$ can be read from Eqs. (50)–(54) in Ref. [33], while for $v_{\text{pole}}$ we use the expression given by Eq. (55) in Ref. [33]. Initial conditions for Eqs. (11)–(14) are discussed in Ref. [23]. In Refs. [12,34], the authors pointed out that in principle a more accurate expression of the radiation-reaction force should not use the Keplerian relation between $r$ and $\omega$ when the binary evolves inside the LSO. However, as also noticed and discussed in Ref. [13], this modification of the radiation-reaction effects has little effect on the waveform amplitude. Since it is not one of the goals of this paper to improve the amplitude agreement between the numerical and EOB waveforms, we do not include it.

The last crucial ingredient of the EOB model is the inclusion of the ringdown phase. After the two BHs merge, the system settles down to a Kerr BH and emits quasinormal modes (QNMs) [35,36]. In the test-mass limit, $\eta \ll 1$, Refs. [36,37] realized that when a test particle falls radially

---

[1]When using the EOB real Hamiltonian we should in principle consider the (generalized) canonical transformation between the real and effective variables which is explicitly given as a PN expansion in Refs. [20,21]. However, since the Hamilton equations are valid in any canonical coordinate system, when we evolve the EOB dynamics we write the Hamilton equations in terms of the effective variables. When comparing to NR results, there might be some differences in the time variable, though. In any case Eqs. (11)–(14) define our EOB model.

below $3M$ (the unstable light ring of Schwarzschild), it immediately triggers the production of QNMs. In the comparable-mass case $\eta \lesssim 1/4$, to approximate the late part of the merger waveforms, Ref. [38] proposed the so-called close-limit approximation, which consists of switching from the two-body description to the one-body description (perturbed BH) close to the light-ring location. Based on these observations, Ref. [20] modeled the merger as a very short (instantaneous) phase and matched the inspiral(-plunge) waveform to a damped sinusoid at the light-ring position. The frequency and decay time were computed estimating the final BH mass and spin from the EOB energy and angular momentum at the matching point. The matching procedure has then been improved, by adding more QNMs, extending it to several multipole moments [7,34], and applying it over a time interval instead of one point in time [13].

## III. PSEUDO 4PN EFFECTIVE-ONE-BODY MODEL

Previous investigations [7,9] focusing on comparable-mass binaries, have shown that a non-negligible dephasing can accumulate at the transition inspiral(-plunge) to ringdown between the 3.5PN-EOB waveform and the NR waveform. The dephasing is caused by the much faster increase of the GW frequency in the 3.5PN-EOB model than in the NR simulation when approaching the light-ring position. Although the dephasing would prevent an accurate determination of the binary parameters in applications to gravitational-wave observations, it would not prevent detection of the signals. In Ref. [9] the authors built *effectual*[2] EOB templates which match the EOB inspiral(-plunge) to ringdown through three parameters. The latter describe the time of matching, and the difference between the final BH mass (spin) and the EOB energy (angular momentum) at the matching point.[3] In this paper we improve on Ref. [9] implementing a matching procedure that does not require the introduction of any new parameter and that agrees with numerical simulation waveforms within a rather small phase difference, $\lesssim 0.08$ of a GW cycle, thus providing accurate or *faithful*[4] templates.

To decrease the differences between the EOB and NR waveforms during the last stages of inspiral and plunge, we introduce a 4PN order term in the effective potential $A(r)$, given by Eq. (5), that is

---

[2]Following Ref. [27], by *effectual* templates we mean templates that have large overlaps, say $\gtrsim 96.5\%$, with the expected signal after maximizing over the initial phase, time of arrival, and BH masses. Effectual templates can be used for detection but may lead to large biases in estimating the binary parameters.

[3]These parameters are not arbitrary. They can be related to the BH masses as long as accurate NR simulations for several BH mass ratios are available.

[4]Following Ref. [27], by *faithful* templates we mean templates that have large overlaps, say $\gtrsim 96.5\%$, with the expected signal maximizing *only* over the initial phase and time of arrival.

$$A_T^{\mathrm{p4PN}}(r) = A_T^{\mathrm{3PN}}(r) + \frac{a_5(\eta)}{r^5}, \qquad (16)$$

and Padé approximate it using the approximant $A_{P_4^1}$. A similar modification was employed in Ref. [30] to obtain better matches of the EOB model to quasiequilibrium initial-data configurations [39] and was also pointed out in Ref. [22]. An interesting motivation for this change is the following [20,23]: From Eq. (12) it is straightforward to write the EOB *instantaneous* frequency as

$$\omega(t) = \frac{A(r)}{r^2} \frac{p_\varphi}{\eta \hat{H}_{\mathrm{real}} \hat{H}_{\mathrm{eff}}}. \qquad (17)$$

It is reasonable to assume that during the plunge, the two-body dynamics is no longer driven by radiation-reaction effects [25], but occurs mostly along a geodesic, with fixed angular momentum $p_\varphi$ and energy $\hat{H}_{\mathrm{real}}$ and $\hat{H}_{\mathrm{eff}}$. Thus, we can write

$$\omega_{\mathrm{plunge}}(t) = \frac{A(r)}{r^2} \mathrm{const}, \qquad (18)$$

$$\mathrm{const} = \left[ \frac{p_\varphi}{\eta \hat{H}_{\mathrm{real}} \hat{H}_{\mathrm{eff}}} \right]_{\mathrm{LSO}}. \qquad (19)$$

The above equations clearly show how the coefficient $A(r)$ determines the frequency during the plunge, i.e., from the LSO until the light-ring position. The latter happens at the maximum of $A(r)/r^2$. A direct test has shown that the relative difference between $\omega_{\mathrm{plunge}}$ and the exact $\omega$ from the EOB-LSO to the light ring is at most 5% in the 4:1 case.

Since the 4PN term has not been calculated in PN theory, we shall denote it as "p4PN," where "p" stands for *pseudo*. We do not claim that when the 4PN order term is calculated it will agree with the p4PN order term. In fact, the latter should be considered as a phenomenological term. We have

$$A_{P_4^1}^{\mathrm{p4PN}}(r) = \frac{\mathrm{Num}(A_{P_4^1}^{\mathrm{p4PN}})}{\mathrm{Den}(A_{P_4^1}^{\mathrm{p4PN}})}, \qquad (20)$$

with

$$\mathrm{Num}(A_{P_4^1}^{\mathrm{p4PN}}) = r^3[32 - 24\eta - 4a_4(\eta, 0) - a_5(\eta, \lambda)]$$
$$+ r^4[a_4(\eta, 0) - 16 + 8\eta], \qquad (21)$$

$$\text{Den}(A^{\text{p4PN}}_{P^1_4}) = -a_4^2(\eta,0) - 8a_5(\eta,\lambda) - 8a_4(\eta,0)\eta + 2a_5(\eta,\lambda)\eta - 16\eta^2$$
$$+ r[-8a_4(\eta,0) - 4a_5(\eta,\lambda) - 2a_4(\eta,0)\eta - 16\eta^2] + r^2[-4a_4(\eta,0) - 2a_5(\eta,\lambda) - 16\eta]$$
$$+ r^3[-2a_4(\eta,0) - a_5(\eta,\lambda) - 8\eta] + r^4(-16 + a_4(\eta,0) + 8\eta), \tag{22}$$

where

$$a_5(\eta,\lambda) = \lambda\eta, \tag{23}$$

and $\lambda$ will be determined by comparison with numerical results. We could also introduce a 4PN order term in the coefficient $D(r)$. However, we find that the effect on the dynamics is relatively small and decide to use the Padé approximant

$$D^{\text{p4PN}}_{P^0_4}(r) = \frac{r^4}{r^4 + 6\eta r^2 + 2\eta(26 - 3\eta)r + 36\eta}. \tag{24}$$

The difference between $D^{\text{p4PN}}_{P^0_4}(r)$ and $D^{\text{3PN}}_{P^0_3}(r)$, Eq. (10), causes a negligible change in all our results.

In the left panel of Fig. 1 we show how the p4PN order term $\lambda$ modifies the position of the EOB LSO and light ring (the last unstable orbit for a massless particle) for several binary mass ratios. Later on we shall see that the value of $\lambda$ that best fits the NR results (see Sec. IV) is $\lambda = 60$. It always guarantees the presence of a LSO and a light ring. Quite interestingly, we notice that Ref. [31] had predicted $0 \lesssim \lambda \lesssim 250$. In the right panel of Fig. 1, we show the circular-orbit energy computed with the EOB Hamiltonian, and the radial potential for a massless particle, at different PN orders with fixed $\lambda = 60$. We notice that the LSO energy ($E^{\text{EOB}}_{\text{p4PN}}/M = -0.0185$) and frequency ($M\omega^{\text{EOB}}_{\text{p4PN}} = 0.1047$) at p4PN order are closer to the corresponding values obtained using the 3PN-Taylor-expanded model for quasicircular adiabatic orbits [40], and to the quasie-quilibrium initial-data approach [41] (see Fig. 16 and

Table II in Ref. [41]). This could be a pure accident. In fact, it should be kept in mind that the LSO frequency computed from the 3PN-Taylor-expanded conservative dynamics is [40] $M\omega^{\text{T}}_{\text{3PN}} \sim 0.129$ ($E^{\text{T}}_{\text{3PN}}/M = -0.0193$), quite close to the formation of the common apparent horizon in the NR simulation, and quite far from the frequency $\sim 0.08$ at which the indistinct plunge occurs [7]. What we can certainly say is that the p4PN-EOB conservative dynamics is closer than at 3PN order to the 3PN Taylor-expanded conservative dynamics of quasicircular adiabatic orbits [40].

## IV. EFFECTIVE-ONE-BODY WAVEFORMS FOR INSPIRAL, MERGER, AND RINGDOWN

Integrating the p4PN-EOB Hamiltonian equations provides a description of the binary's dynamical evolution. As described below, we derive our waveforms directly from the EOB dynamics until the system approaches the light ring. Thereafter we complete each spherical harmonic waveform component by matching it to a set of quasinormal ringdown modes. Because the ringdown mode frequencies depend on the mass $M_f$ and spin parameter $a_f$ of the final BH formed by the merger, this part of the model will require an additional prescription for accurately determining these values.

Following the tradition in NR we describe the waveforms in terms of a spin-weighted spherical harmonic decomposition. From our numerical simulations we directly compute the Weyl tensor $\Psi_4$, which in terms of
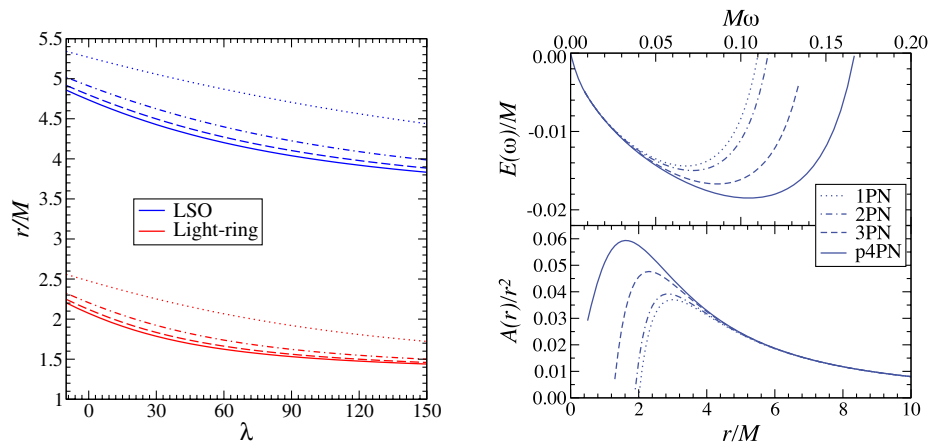


FIG. 1 (color online). In the left panel we show the position of the LSO and light ring as function of the parameter $\lambda$, for different mass ratios: 4:1 (dotted line), 2:1 (dot-dashed line), 3:2 (dashed line), and 1:1 (continuous line). In the right panel we show: (top part) the energy for circular orbits as a function of the frequency evaluated from the EOB Hamiltonian, (bottom part) the radial potential as function of the radial coordinate for a massless particle in the EOB model. The various curves refer to different PN orders.

spin-weight $-2$ spherical harmonics $_{-2}Y_{lm}(\theta, \phi)$ [42] reads [see Ref. [43] for details]

$$MR\Psi_4 = \sum_{lm} {}_{-2}C_{lm}(t)_{-2}Y_{lm}(\theta, \phi), \tag{25}$$

$R$ being the extraction radius. In terms of the $+$ and $\times$ GW polarizations we have[5]

$$\Psi_4 = -(\ddot{h}_+ - i\ddot{h}_\times). \tag{26}$$

Thus, we can write

$$_{-2}C_{lm} = -MR \int d\Omega_{-2}Y_{lm}^*(\theta, \phi)(\ddot{h}_+ - i\ddot{h}_\times). \tag{27}$$

In the adiabatic approximation ($\dot{\omega}/\omega^2 \ll 1$), we obtain

$$_{-2}C_{lm} = -MRm^2\omega^2 h_{lm}, \tag{28}$$

where

$$h_{lm} \equiv -(h_+ - ih_\times)_{lm}$$
$$= -\int d\Omega_{-2}Y_{lm}^*(\theta, \phi)(h_+ - ih_\times). \tag{29}$$

We compute the EOB $h_{lm}$ in the so-called restricted approximation, i.e., at leading order in the PN expansion. They read:

$$\frac{M}{R}h_{21}^{\rm EOB} = -\frac{8}{3}\sqrt{\frac{\pi}{5}}\frac{\delta m}{M}\eta(M\omega)e^{-i\varphi}, \tag{30}$$

$$\frac{M}{R}h_{22}^{\rm EOB} = -8\sqrt{\frac{\pi}{5}}\eta(M\omega)^{2/3}e^{-2i\varphi}, \tag{31}$$

$$\frac{M}{R}h_{31}^{\rm EOB} = -\frac{2}{3}\sqrt{\frac{\pi}{70}}\eta\frac{\delta m}{M}(M\omega)e^{-i\varphi}, \tag{32}$$

$$\frac{M}{R}h_{32}^{\rm EOB} = -\frac{8}{3}\sqrt{\frac{\pi}{7}}\eta(1 - 3\eta)(M\omega)^{4/3}e^{-2i\varphi}, \tag{33}$$

$$\frac{M}{R}h_{33}^{\rm EOB} = -3\sqrt{\frac{6\pi}{7}}\frac{\delta m}{M}\eta(M\omega)e^{-3i\varphi}, \tag{34}$$

$$\frac{M}{R}h_{42}^{\rm EOB} = -\frac{8}{63}\sqrt{\pi}\eta(1 - 3\eta)(M\omega)^{4/3}e^{-2i\varphi}, \tag{35}$$

$$\frac{M}{R}h_{44}^{\rm EOB} = -\frac{64}{9}\sqrt{\frac{\pi}{7}}\eta(1 - 3\eta)(M\omega)^{4/3}e^{-4i\varphi}, \tag{36}$$

where $\delta m = m_1 - m_2 > 0$, and $\varphi$ is the binary orbital phase. Note that $h_{l-m} = (-1)^l h_{lm}^*$. The RD modes are attached at the time when the orbital frequency reaches

its maximum and this occurs slightly before the light-ring position, $r_{\rm match} = 1.651$, $M\omega = 0.1883$ ($\eta = 0.25$) and $r_{\rm match} = 2.089$, $M\omega = 0.1665$ ($\eta = 0.16$). It is useful to have an analytic formula relating the maximum of the orbital frequency, i.e., the matching point, to $\eta$. A simple fit gives

$$M\omega_{\rm match} = 0.133 + 0.183\eta + 0.161\eta^2. \tag{37}$$

We find that the above fitting has $<0.35\%$ error comparing to numerical values in the range $\eta = 0.05$–$0.25$. The matching to QNMs is obtained by imposing the continuity of $h_{lm}(t)$ and all the higher time derivatives needed to fix the six unknown amplitudes and phases of the three RD modes [7,23]. Following Ref. [7], we attach the fundamental mode, and two overtones. We find that the matching performance does not improve significantly if we add more overtones. The frequency and decay time of the RD modes are computed using the mass $M_f$ and spin $a_f$ of the final BH, using Refs. [45].

For nonspinning binary systems, it is now possible to determine how the final-BH mass and spin depend on the mass ratio. Here we apply an empirical estimate for the functions $M_f(\eta)$ and $a_f(\eta)$ based on a combination of numerical simulations in the range $\eta > 0.16$ and expectations from the test particle limit $\eta \to 0$. In Table I we list the final BH masses and spins for $\eta = 0.25, 0.24, 0.22, 0.16$, extracted from the NR simulations. The values are compatible with Refs. [46,47]. The final mass was computed from the difference of the total radiated energy and the initial ADM mass. To obtain the final spin of the merged BH we first calculate the complex QNM frequency of the $l = 2$, $m = 2$ mode by a linear fit to the phase and log amplitude; the two slopes give the real and imaginary parts of the frequency which are uniquely related to the final spin [45].

In the absence of NR results, to determine the final BH masses and spins to lower values of $\eta$ we apply a fit to the data $\eta = 0.25, 0.24, 0.22, 0.16$. For the BH mass we consider the one-parameter fit function $M_f/M = 1 + (\sqrt{8/9} - 1)\eta - 0.498(\pm 0.027)\eta^2$, where the coefficient of the linear term in $\eta$ has been fixed to the test-mass limit value. For the BH spin we employ the one-parameter fit function $a_f/M_f = \sqrt{12}\eta - 2.900(\pm 0.065)\eta^2$, where again the linear term in $\eta$ has been fixed to the test-mass limit prediction. If we were using a two-parameter fit we would obtain $M_f/M = 1 - 0.024(\pm 0.057)\eta - 0.641(\pm 0.249)\eta^2$, and $a_f/M_f = 3.29(\pm 0.08)\eta - 2.13(\pm 0.33)\eta^2$. We notice that the value of 3.29 is quite close to the LSO angular momentum for a test particle in Schwarzschild, i.e., $\sqrt{12} \simeq 3.4641$ [46]. However, since the two-parameter fit gives larger errors for the BH mass with respect to the one-parameter fit, we stick with the latter. The extrapolation to smaller values of $\eta$ is consistent with the values obtained in Ref. [46] using NR simulations, also

---

[5]Note that this definition of $\Psi_4$ is tetrad-dependent. Here we assume the tetrad given in Ref. [44], Eqs. (5.6). It is also common for $\Psi_4$ to be scaled according to an asymptotically Kinnersley tetrad [Ref. [44], Eqs. (5.9)] which introduces a factor of 2 as in Ref. [43].

TABLE I.   For several values of $\eta$, we list in the second and third columns the values of $M_f/M$ and $a_f/M_f$ computed from the energy released and by extracting the fundamental QNM from $_{-2}C_{22}$, respectively. In the fourth and fifth columns we list the values obtained using the one-parameter fits $M_f/M = 1 + (\sqrt{8/9} - 1)\eta - 0.498(\pm0.027)\eta^2$, and $a_f/M_f = \sqrt{12}\eta - 2.900(\pm0.065)\eta^2$, where the terms linear in $\eta$ have been fixed to the test-mass limit values. In the last two columns we list the values from the Jena group (see Table V of Ref. [46]). Note that the Jena mass values are scaled differently, against ADM mass, $M_o$ of the system at the beginning of the numerical simulations, which should result slightly larger values.

| $\eta$ | $[M_f/M]_{\text{Goddard}}$ | $[a_f/M_f]_{\text{Goddard}}$ | $[M_f/M]_{\text{fit}}$ | $[a_f/M_f]_{\text{fit}}$ | $[M_f/M_o]_{\text{Jena}}$ | $[a_f/M_f]_{\text{Jena}}$ |
|---|---|---|---|---|---|---|
| 0.25 | 0.9526 | 0.687 | 0.9546 | 0.685 | 0.9628 | 0.684 |
| 0.24 | 0.9561 | 0.670 | 0.9576 | 0.664 | 0.9660 | 0.664 |
| 0.2222 | 0.9668 | 0.621 | 0.9633 | 0.623 | 0.9714 | 0.626 |
| 0.2041 | $\cdots$ | $\cdots$ | 0.9676 | 0.586 | 0.9762 | 0.581 |
| 0.1875 | $\cdots$ | $\cdots$ | 0.9618 | 0.548 | 0.9800 | 0.544 |
| 0.1728 | $\cdots$ | $\cdots$ | 0.9752 | 0.512 | 0.9831 | 0.509 |
| 0.16 | 0.9783 | 0.472 | 0.9781 | 0.480 | 0.9855 | 0.478 |
| 0.12 | $\cdots$ | $\cdots$ | 0.9860 | 0.374 | $\cdots$ | $\cdots$ |
| 0.08 | $\cdots$ | $\cdots$ | 0.9922 | 0.259 | $\cdots$ | $\cdots$ |
| 0.04 | $\cdots$ | $\cdots$ | 0.9969 | 0.134 | $\cdots$ | $\cdots$ |
| 0.01 | $\cdots$ | $\cdots$ | 0.9994 | 0.034 | $\cdots$ | $\cdots$ |

listed in Table I, and in Ref. [24] using a combination of test-mass limit predictions and the EOB approach. Henceforth, when computing the frequency and decay time of the QNMs we use the results obtained from the one-parameter fit in Table I.

This completes the specification of our waveform model, which can be applied to provide full waveform predictions for noneccentric and nonspinning binary BH mergers of arbitrary mass ratio.

## V. COMPARISON WITH NUMERICAL RELATIVITY

In this section we examine how closely our model waveforms fit with the results of our numerical simulations. While we have already applied some limited information from these numerical simulations in defining our model, such as in deriving our functional fits for $M_f(\eta)$ and $a_f(\eta)$ and in selecting the optimal value for $\lambda$, we can now compare the full waveforms. In particular, though our

model was developed primarily in consideration of the $h_{22}$ waveforms, we find here that other multipolar waveform components are also well described.

To measure the differences between the NR and EOB waveforms we compute the *fitting factor* (FF), or ambiguity function [9,27,33]. We recall that the overlap $\langle h_1(t), h_2(t)\rangle$ between the waveforms $h_1(t)$ and $h_2(t)$ is defined by

$$\langle h_1(t), h_2(t)\rangle \equiv 4\,\mathrm{Re}\int_0^\infty \frac{\tilde{h}_1(f)\tilde{h}_2^*(f)}{S_h(f)}\,df, \qquad (38)$$

where $\tilde{h}_i(f)$ is the Fourier transform of $h_i(t)$, and $S_h(f)$ is the detector's power spectral density (PSD). The FF is the normalized overlap between the NR waveform $h^{\text{NR}}(t)$ (target) and the EOB waveform $h^{\text{EOB}}(t_0, \varphi_0)$ (template) maximized *only* over the initial time $t_0$ and initial phase $\varphi_0$, and minimized over the initial phase $\varphi$ of the target (the so-called minmax [27]), that is

$$\mathrm{FF} \equiv \min_\varphi \max_{t_0,\varphi_0} \frac{\langle h^{\text{NR}}(\varphi; \lambda^i), h^{\text{EOB}}(t_0, \varphi_0; \lambda^i)\rangle}{\sqrt{\langle h^{\text{NR}}(\varphi; \lambda^i), h^{\text{NR}}(\varphi; \lambda^i)\rangle\langle h^{\text{EOB}}(t_0, \varphi_0; \lambda^i), h^{\text{EOB}}(t_0, \varphi_0; \lambda^i)\rangle}}, \qquad (39)$$

where $\lambda^i$ are the binary parameters. For the detector PSD we shall consider either white noise or the LIGO noise.

The equal-mass run lasts for ~14 GW cycles before merger. This run was published originally in Refs. [8,43], and further studied for data-analysis purposes in Ref. [9]. The unequal-mass runs, $m_1/m_2 = 3/2, 2, 4$, last for 5, 5, and 9 GW cycles before merger. The $m_1/m_2 = 3/2, 2$ cases were published in Refs. [9,10] and the $m_1/m_2 = 4$ has recently been computed by the NASA-Goddard group. Adaptive mesh refinement was employed for this case as in

the previous simulations, with a finest mesh resolution of $h_m = 3M/160$ used in one run and $h_h = M/64$ used in a second. Adequate convergence of the Hamiltonian and momentum constraints were found; the numerical details will be reported in a future publication. Based on the comparisons between high- and medium-resolution waveforms, we estimated in Ref. [9] the FFs between high resolution and exact waveforms for the $m_1/m_2 = 1$ case. Here we apply the same procedure for the $m_1/m_2 = 4$ case. If we have several simulations with different resolu-

tions, specified by the mesh spacings $x_i$, and $x_i$ are sufficiently small, we can assume that the waveforms $h_i$ are given by

$$h_i = h_0 + x_i^n h_d, \tag{40}$$

where $n$ is the convergence factor of the waveform, $h_0$ is the exact waveform generated from the infinite resolution run ($x_0 \rightarrow 0$), and $h_d$ is the leading order truncation error contribution to the waveform and is independent of the mesh spacing $x_i$. The mismatch between the waveforms $h_i$ and $h_j$, $1 - \mathrm{FF}_{ij}$, then scales as

$$1 - \mathrm{FF}_{ij} \propto (x_i^n - x_j^n)^2. \tag{41}$$

In the Goddard simulations, the high and medium resolution runs have mesh-spacing ratio $x_h/x_m = 5/6$, and the waveform convergence rate was shown to be $n = 4$ in the 1:1 case [43]. The FF between the high resolution and

exact waveforms $h_h$ and $h_0$ is given by

$$\mathrm{FF}_{0h} = 1 - 0.87(1 - \mathrm{FF}_{hm}), \tag{42}$$

where $\mathrm{FF}_{hm}$ is the FF between the high and medium resolution waveforms $h_h$ and $h_m$. Thus, the mismatch between $h_h$ and $h_0$ is slightly smaller than that between $h_h$ and $h_m$, where the latter can be derived from the FFs shown in the left panel of Fig. 2 computed using LIGO's PSD. If we use white noise we find FF = 0.9922 and = 0.9920 for mass ratios 1:1 and 4:1, respectively. Henceforth, we shall always use high-resolution waveforms for the $m_1/m_2 = 4$ and 1 cases.

For different mass ratios, we show in the right panel of Fig. 2 how the FF computed for the dominant modes, using white noise, depends on the parameter $\lambda$. Based on this plot we identified $\lambda = 60$ as the best model, which we use in the rest of the paper.
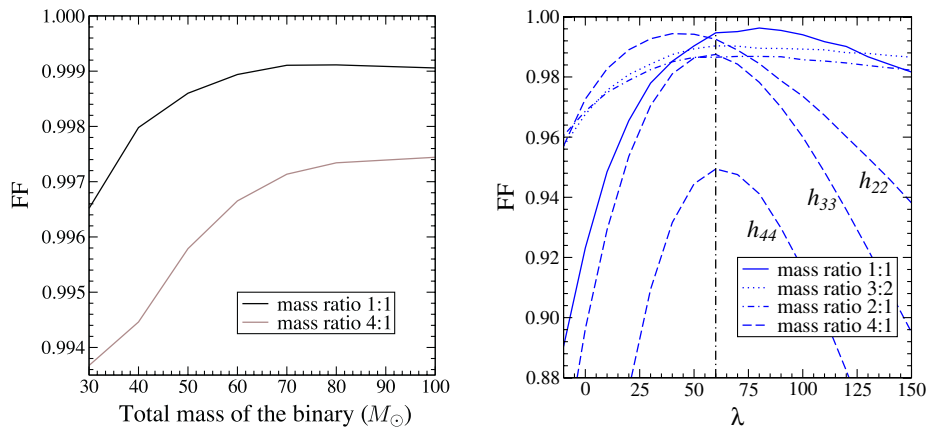


FIG. 2 (color online). In the left panel we show the (minmax) FF between the high and medium resolution runs, $\langle h^{\mathrm{NR,h}}, h^{\mathrm{NR,m}} \rangle$, as a function of the binary total mass $M$. The FFs are evaluated using LIGO's PSD. If we use white noise we find 0.9922 and 0.9920 for mass ratios 1:1 and 4:1, respectively. In the right panel, for different mass ratios, we show how the (minmax) FF $\langle h^{\mathrm{NR}}, h^{\mathrm{EOB}} \rangle$ (computed using white noise) depends on the parameter $\lambda$. For mass ratios 1:1, 2:1, and 3:2 we compute $\langle h_{22}^{\mathrm{NR}}, h_{22}^{\mathrm{EOB}} \rangle$, while for 4:1 we show also results for $\langle h_{33}^{\mathrm{NR}}, h_{33}^{\mathrm{EOB}} \rangle$ and $\langle h_{44}^{\mathrm{NR}}, h_{44}^{\mathrm{EOB}} \rangle$. The vertical line refers to the value $\lambda = 60$ which we employ in all subsequent analyses.
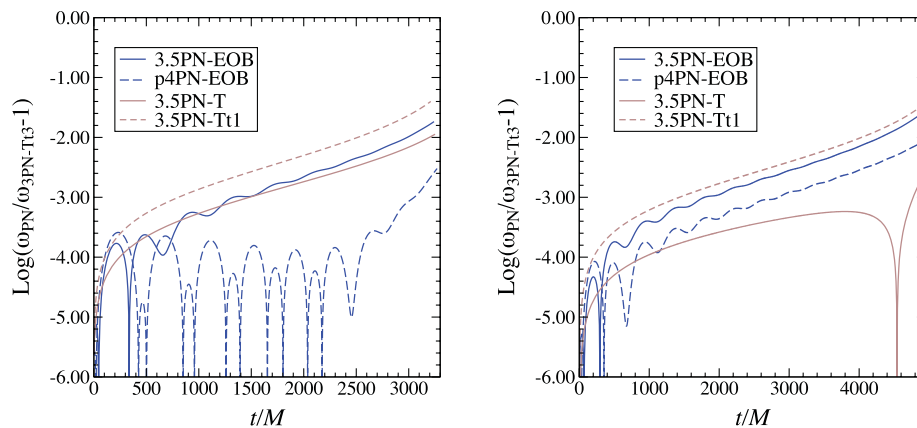


FIG. 3 (color online). We show the differences in the orbital frequency between the 3.5PN-Tt3 model and 3.5PN-T, 3.5PN-Tt1, 3.5PN-EOB, p4PN-EOB models for mass ratios 1:1 (left panel) and 4:1 (right panel). The PN frequencies coincide at $\omega M = 0.017$ at $t = 0$, and end at $\omega M = 0.035$.

The p4PN-EOB model has better matching performances at the inspiral-merger-ringdown transition. However, the introduction of the 4PN order term inevitably affects the inspiral waveform. To understand the differences between the p4PN-EOB model and NR and other PN models during the long *inspiral phase* we plot in Fig. 3 the frequency difference between several PN approximants. Because preliminary results from Caltech/Cornell group suggest that the 3PN-Tt3 approximant model fits well with an accurate $3000M$-long equal-mass simulation [48], we use this as the fiducial PN model. The 3.5PN-T, 3PN-Tt3 and 3.5Tt1 models are the so-called Taylor-expanded PN models, widely used in the data-analysis literature (see, e.g., Refs. [9,33,49]). The plots are obtained by imposing that the PN frequencies agree at $\omega M = 0.017$. The 3PN-Tt3 model is an analytic model that uses the PN-expanded phase as function of time. It was also used in Ref. [7] [see Eq. (31) there], where it was found to best match (together with the 3.5PN-T model) the equal-mass waveform computed with generalized harmonic coordinates. The 3.5PN-T model uses the energy balance equation reexpanded in powers of the orbital frequency. It was found to best match the equal-mass waveforms in Refs. [7–9]. The 3.5PN-Tt1 model is a numerical PN model that solves the energy balance equation without reexpanding the flux and energy function, as done in the 3.5PN-T model. The 3.5PN-Tt1 model was recently used by the Jena group [11] to compare with equal-mass waveforms computed with the moving puncture code. From the plots we conclude that while for the equal-mass case the p4PN-EOB model is rather close to our fiducial model (and thus to preliminary results from long numerical simulations), we cannot draw definite conclusions for generic mass ratios. Indeed, the right panel in Fig. 3 shows that for unequal masses, the closeness of the PN approximants is different than in the equal-mass case.

In Figs. 4–6 we show the comparison between the p4PN-EOB and NR waveforms, orbital frequencies, and phase differences for the most accurate, long numerical
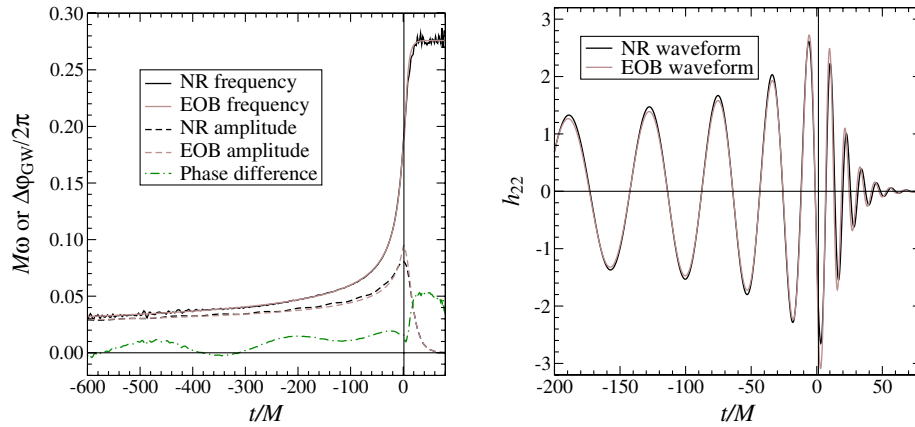


FIG. 4 (color online). Equal-mass binary. In the left panel we plot the NR and p4PN-EOB frequencies and amplitudes, and the phase difference between the EOB and NR $h_{22}$. In the right panel we compare the EOB and NR $h_{22}$. We maximize only on the initial phase and time of arrival. Note that we show only the last few cycles. The complete inspiral waveform has 14 GW cycles.
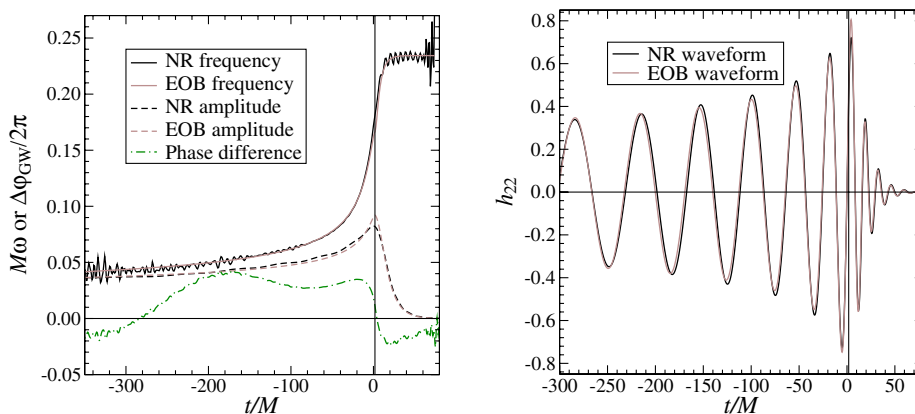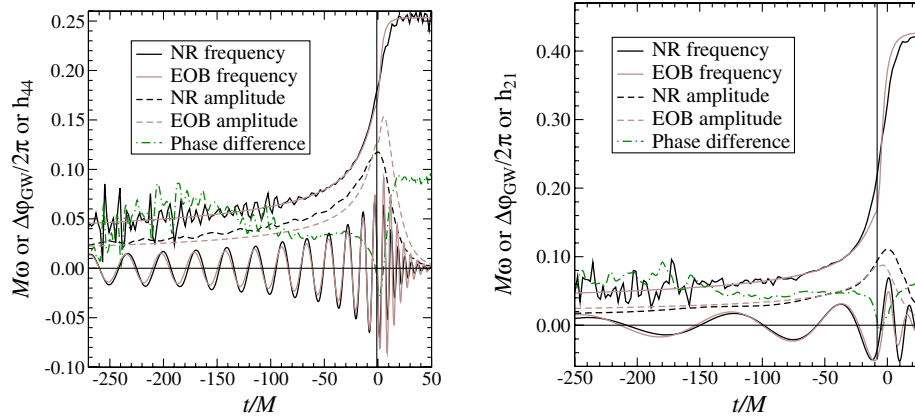


FIG. 5 (color online). Binary with mass ratio 4:1. In the left panel we plot the NR and p4PN-EOB frequencies and amplitudes, and the phase difference between the EOB and NR $h_{22}$. In the right panel we compare the EOB and NR $h_{22}$. We maximize only over the initial phase and time of arrival. Note that we show only the last few cycles. The complete inspiral waveform has 9 GW cycles.

FIG. 6 (color online). Binary with mass ratio 4:1. In the left (right) panel we compare the p4PN-EOB and NR $h_{44}$ ($h_{21}$). We maximize only on the initial phase and time of arrival.

simulations, notably the 1:1 and 4:1 cases. We show results for the $l = 2$, $m = 2$ mode, and also for the $l = 4$, $m = 4$ and $l = 2$, $m = 1$ modes. The p4PN-EOB $l = 3$, $m = 3$ mode matches rather well the NR mode, similarly to the $l = 2$, $m = 2$ case, thus we do not show it. When the mass ratio increases the other modes are no longer so subdominant with respect to the $l = 2$, $m = 2$ mode, as seen in the right panel of Fig. 8. In the Appendix we present similar plots for the $l = 2$, $m = 2$ mode of the shorter runs with mass ratios 2:1 and 3:2.

In Tables II, III, and IV we list the FFs and the phase difference (in one GW cycle) between several p4PN-EOB modes and the NR modes, for white noise and LIGO's PSD, respectively. The dominant frequencies associated with each $l$, $m$ mode are rather similar all along the inspiral, as seen in the left panel of Fig. 8. However, due to the different frequency of the fundamental QNM [10], the frequencies associated with the $l = 2$, $m = 1$ and $l = 3$, $m = 2$ modes decouple from the other frequencies during the transition inpiral(-plunge) to ringdown.

Tables II and III show that the FFs are rather high except for a few modes, like the $l = 4$, $m = 4$ mode with mass ratio 4:1 [see the left panel in Fig. 6]. In this case we find that our matching procedure is not so efficient in reproducing the amplitude of the NR ringdown waveform. More

TABLE III. For several mass configurations, we list the (minmax) FFs obtained using LIGO's PSD and maximizing only on the time of arrival and initial phase, and the phase difference in one GW cycle.

| $(m_1 + m_2)$ | $lm$ | $\langle h_{lm}^{\mathrm{NR}}, h_{lm}^{\mathrm{p4PN-EOB}} \rangle$ | $\Delta\varphi_{\mathrm{GW}}/(2\pi)$ |
|---|---|---|---|
| $(15 + 15)M_\odot$ | 22 | 0.9975 | ±0.043 |
| $(50 + 50)M_\odot$ | 22 | 0.9817 | ±0.043 |
| $(20 + 30)M_\odot$ | 22 | 0.9897 | ±0.065 |
| $(20 + 40)M_\odot$ | 22 | 0.9889 | ±0.068 |
| $(10 + 40)M_\odot$ | 22 | 0.9961 | ±0.035 |
| $(10 + 40)M_\odot$ | 33 | 0.9911 | ±0.055 |
| $(10 + 40)M_\odot$ | 44 | 0.9720 | ±0.075 |
| $(10 + 40)M_\odot$ | 21 | 0.9737 | ±0.080 |
| $(20 + 80)M_\odot$ | 22 | 0.9965 | ±0.035 |
| $(20 + 80)M_\odot$ | 33 | 0.9873 | ±0.055 |
| $(20 + 80)M_\odot$ | 44 | 0.9548 | ±0.065 |
| $(20 + 80)M_\odot$ | 21 | 0.9804 | ±0.125 |

TABLE II. For several mass configurations, we list the (min-max) FF obtained using white noise and maximizing only on the time of arrival and initial phase, and the phase difference in one GW cycle. For comparison, using the 3.5PN-EOB model we find $\langle h_{22}^{\mathrm{NR}}, h_{22}^{3.5\mathrm{PN-EOB}} \rangle = 0.8718$ and $= 0.9569$ for mass ratios 1 and 4, respectively.

| $\eta$ | $lm$ | $\langle h_{lm}^{\mathrm{NR}}, h_{lm}^{\mathrm{p4PN-EOB}} \rangle$ | $\Delta\varphi_{\mathrm{GW}}/(2\pi)$ |
|---|---|---|---|
| 0.25 | 22 | 0.9907 | ±0.030 |
| 0.24 | 22 | 0.9881 | ±0.058 |
| 0.22 | 22 | 0.9878 | ±0.078 |
| 0.16 | 22 | 0.9925 | ±0.035 |
| 0.16 | 33 | 0.9860 | ±0.055 |
| 0.16 | 44 | 0.9436 | ±0.065 |
| 0.16 | 21 | 0.9092 | ±0.050 |

TABLE IV. Binary with mass-ratio 4:1. For several inclinations angles, we list the (minmax) FFs between the p4PN-EOB and NR waveforms, given by Eq. (43), using white noise. In all cases the fitting factor exceeds 0.98.

| $\theta$ | $\langle h_+^{\mathrm{NR}}, h_+^{\mathrm{p4PN-EOB}} \rangle$ | $\langle h_\times^{\mathrm{NR}}, h_\times^{\mathrm{p4PN-EOB}} \rangle$ |
|---|---|---|
| 0 | 0.9925 | 0.9925 |
| $\pi/6$ | 0.9915 | 0.9917 |
| $\pi/4$ | 0.9890 | 0.9900 |
| $\pi/3$ | 0.9854 | 0.9883 |
| $\pi/2$ | 0.9803 | $\cdots$ |

studies extended to different mass ratios may shed light on this anomaly. The $l = 3$, $m = 2$ mode contains a mode mixing between the $l = 2$, $m = 2$ and $l = 3$, $m = 2$ modes [7], and the matching procedure that we adopt does not accurately reproduce it. Better knowledge of how these modes are excited during the inspiral to ringdown transition is required to solve this problem. Finally, because the dominant frequency associated with the $l = 2$, $m = 1$ mode departs from the dominant frequency associated with the $l = 2$, $m = 2$ mode quite before the merger (see the left panel in Fig. 8), and it rises to a much higher QNM

frequency, we find that the FF associated with the $l = 2$, $m = 1$ mode is not very high. In fact, our matching procedure is optimized to reproduce the increase of frequency of the dominant $l = 2$, $m = 2$ and $l = 3$, $m = 3$ modes.

While the FFs listed in Tables II and III are obtained maximizing *independently* over the phase and time of arrival of each $l$, $m$ mode, the FFs in Table IV are computed by matching the full waveform containing all together the leading modes (see Fig. 8). To achieve this we build the numerical and EOB expressions for

$$
\begin{aligned}
h(\theta, \phi; t_0, \varphi_0; \lambda_i) &\equiv -(h_+ - ih_\times), \\
&= {}_{-2}Y_{21}(\theta, \phi)h_{21}(t_0, \varphi_0; \lambda_i) + {}_{-2}Y_{22}(\theta, \phi)h_{22}(t_0, \varphi_0; \lambda_i) + {}_{-2}Y_{31}(\theta, \phi)h_{31}(t_0, \varphi_0; \lambda_i) \\
&\quad + {}_{-2}Y_{32}(\theta, \phi)h_{32}(t_0, \varphi_0; \lambda_i) + {}_{-2}Y_{33}(\theta, \phi)h_{33}(t_0, \varphi_0; \lambda_i) + {}_{-2}Y_{42}(\theta, \phi)h_{42}(t_0, \varphi_0; \lambda_i) \\
&\quad + {}_{-2}Y_{44}(\theta, \phi)h_{44}(t_0, \varphi_0; \lambda_i) + {}_{-2}Y_{2-1}(\theta, \phi)h_{2-1}(t_0, \varphi_0; \lambda_i) + {}_{-2}Y_{2-2}(\theta, \phi)h_{2-2}(t_0, \varphi_0; \lambda_i) \\
&\quad + {}_{-2}Y_{3-1}(\theta, \phi)h_{3-1}(t_0, \varphi_0; \lambda_i) + {}_{-2}Y_{3-2}(\theta, \phi)h_{3-2}(t_0, \varphi_0; \lambda_i) + {}_{-2}Y_{3-3}(\theta, \phi)h_{3-3}(t_0, \varphi_0; \lambda_i) \\
&\quad + {}_{-2}Y_{4-2}(\theta, \phi)h_{4-2}(t_0, \varphi_0; \lambda_i) + {}_{-2}Y_{4-4}(\theta, \phi)h_{4-4}(t_0, \varphi_0; \lambda_i),
\end{aligned}
\tag{43}
$$

and maximize over the template time of arrival $t_0$ and initial phase $\varphi_0$. The waveform seen by an interferometer GW detector is the linear combination of the two polarization states $h_+$ and $h_\times$ defined in the radiation frame, with the combination coefficients given by the polarization angle $\alpha$, as $\cos\alpha$ and $\sin\alpha$ (see e.g., Ref. [6]). Since in Eq. (43) the $h_{lm}$ modes have different dependence on $\varphi_0$, the polarization angle $\alpha$ cannot be absorbed into $\varphi_0$, as done when considering only the dominant $l = 2$, $m = 2$ mode. In principle, we should consider (target) numerical signals with different values of $\alpha$ and maximize the EOB template over $\alpha$. However, since we shall find that both $h_+$ and $h_\times$ can be matched with high FFs by the p4PN-EOB templates, it is not likely that different values of $\alpha$ will reduce the FFs significantly.

To reproduce $h_+$ and $h_\times$ through 1PN order as given by Ref. [50], we would need to add the next-to-leading PN correction to $h_{22}$ in Eq. (30), that is we need to multiply Eq. (30) by $[1 + (55\eta - 107)/42\omega^{2/3}]$, and insert Eqs. (30)–(36) in Eq. (43). After checking that the next-to-leading correction to $h_{22}$ has a tiny effect on the FF, and that also the contribution of the modes $h_{32}$, $h_{31}$, and $h_{42}$ is rather small, we compute the FFs restricting Eq. (43) to the dominant modes $h_{22}$, $h_{33}$, $h_{44}$, and $h_{21}$. The figures listed in Table IV refer to different inclination angles. Despite the fact that the $l = 4$, $m = 4$ mode is recovered only with FF $\sim 0.95$ and the $l = 2$, $m = 1$ mode is recovered only with FF $\sim 0.90$ (see Tables II and III), the FFs obtained by combining all the modes are rather high. This happens because the amplitude of the $l = 4$, $m = 4$ and $l = 2$, $m = 1$ modes are much lower than the amplitude of the $l = 2$, $m = 2$ and $l = 3$, $m = 3$ modes, as seen in Fig. 8. In Fig. 7

we plot the 4PN-EOB and NR $h_+$ waveforms for the case of inclination angle $\theta = \pi/3$.

The waveforms shown in Figs. 2 and 4–7, are *normalized* waveforms. In the right panel of Fig. 8, we compare the NR and EOB restricted-approximated amplitudes for several $l$ and $m$ modes. By restricted-approximated amplitude we mean that for each $l$ and $m$ we restrict ourselves to
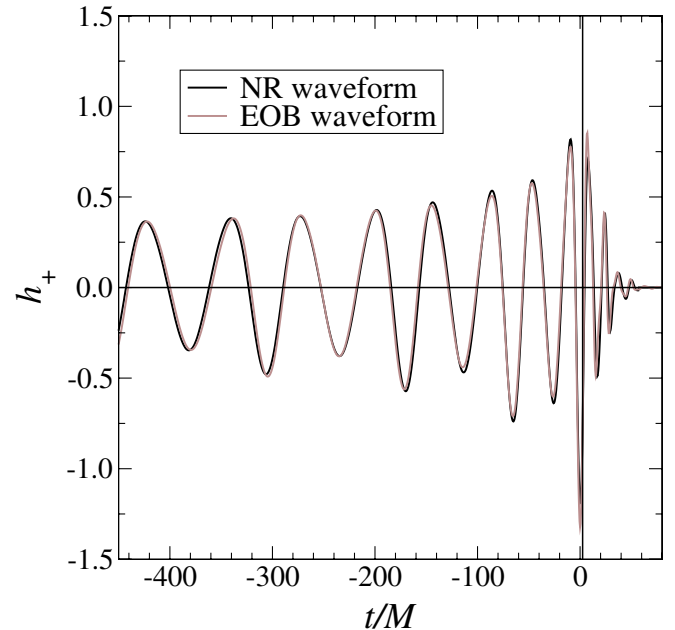


FIG. 7 (color online).   Binary with mass ratio 4:1. We compare the p4PN-EOB and NR $h_+$, given by Eq. (43), extracted at inclination angle $\theta = \pi/3$, maximizing only over the initial phase and time of arrival.
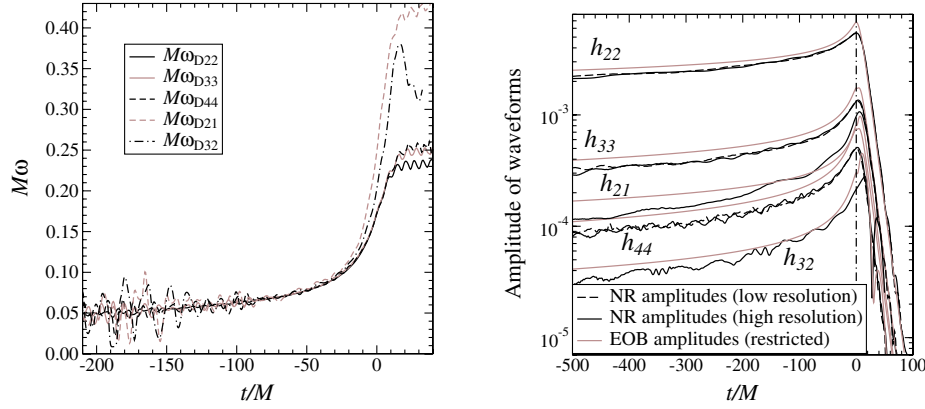
FIG. 8 (color online). Binary with mass ratio 4:1. In the left panel we plot the dominant frequencies for several *l* and *m* modes. Generalizing Eq. (23) in Ref. [7], we define $\omega_{Dlm} = -(1/m)\,\mathrm{Im}(_{-2}\dot{C}_{lm}/_{-2}C_{lm})$ [10]. In the right panel we compare the NR amplitude and EOB restricted-approximated amplitude for several *l* and *m* modes. By restricted-approximated amplitude we mean that for each *l* and *m* we restrict ourselves to the leading order term as given by Eqs. (30)–(36).

the leading order term in the PN expansion [see Eqs. (30)–(36)]. We notice, as already pointed out in Ref. [9], a non-negligible difference between the NR and EOB amplitude. Higher-order PN corrections in the amplitude could in part nullify the difference [11,43], but due to the oscillatory behavior of the higher PN corrections [7], it is hard to draw a robust conclusion. Moreover, there could be a systematic error in the numerical amplitude due to extraction radius. From Fig. 8 we see that amplitudes computed at different resolutions do not affect the amplitude significantly. Although, the difference in the amplitudes has negligible effects on the FFs [9], it may affect the binary parameter estimation and the prediction of the recoil velocity from merging binary BHs [10], thus it needs to be sorted out.

The difference in amplitudes also affects the energy and angular momentum released during the ringdown. We could scale the EOB amplitude by a constant factor and get the same energy and angular momentum as in the NR simulation at the time the ringdown waveform is attached. However, we find that the amount of mass and angular momentum released during the ringdown stage is always larger than the values predicted by NR, as can be seen from the amplitudes shown in the left panels of Figs. 4 and 5. Therefore, the mass and spin of the final BH computed from the EOB model itself are always smaller than the values predicted by NR. For example considering the $h_{22}$ mode, we find that the EOB model underestimates the final mass and spin of the BH by ~2% and ~8%. To resolve this inconsistency, the EOB amplitudes in both the inspiral and ringdown phases would need to be improved. Consequently, we also notice that if we used a *bootstrap* mechanism to locate the EOB matching point between inspiral and ringdown, we would find that the EOB matching must occur too early in time to compensate the fact that the EOB model overestimates the energy and angular momentum released during the ringdown. Such an early matching point would cause a significant phase difference between the EOB and NR waveforms.

## VI. CONCLUSIONS

In this paper we have begun to exploit the flexibility of the EOB approach [22,31] to analytically encode information from numerical-relativity simulations, in order to build faithful templates for binary black holes. By faithful templates [27] we mean templates that have large overlaps, say $\gtrsim 96.5\%$, with the expected signal achieved by maximizing *only* over the initial phase and time of arrival. Thus, they can be employed for detection and parameter estimation.

We have built accurate waveforms by improving the EOB model as follows: We add a p4PN-order term $\lambda\eta$ ($\lambda = 60$) to the EOB coefficient $A(r)$, and Padé approximate the latter to guarantee the presence of the LSO and the light ring [21]. Note that the inclusion of a 4PN term in the coefficient $A(r)$ was employed in Ref. [30] to better fit the EOB model to quasiequilibrium initial-data configurations [39], and was also used to determine the span of EOB templates at 4PN order in Ref. [31]. The choice $\lambda = 60$ found in this paper provides better agreement between the EOB and NR GW frequency associated with the $l = 2$, $m = 2$ mode during the transition inspiral(-plunge) to ringdown. The complete waveform, given by Eqs. (30)–(36) and (43), is then built by evolving Eqs. (11)–(14) throughout the inspiral(-plunge) and attaching three QNMs at the peak of the p4PN-EOB GW frequency, as determined by Eq. (37). The QNM frequency and decay time are fixed by the final BH mass and spin, which can be predicted by extrapolating sparse NR results through a fit which meets expectations for the test-mass limit (see Table I). This is distinct from other approaches based on the EOB model itself [24]. Our general approach remains flexible, allowing the possibility of future improvements.

Although we have tested the accuracy of the p4PN-EOB model for mass ratios $\eta = 0.25$, 0.24, 0.22, and 0.16, our procedure also predicts the waveforms for values of $\eta <$ 0.16, that can be tested against numerical simulations when

accurate, long waveforms become available. Currently, for all cases considered we obtain phase differences with the NR waveforms of less than $\pm 8\%$ in a GW cycle. This result refers to waveforms containing at most 14 GW cycles. To test the performances of the p4PN-EOB model during the long inspiral phase, we compared this model with other PN approximants which fit rather well extremely accurate NR simulations (see Fig. 3). Before merger, in the equal-mass case, the p4PN-EOB model is rather close to the 3PN-Tt3 model which may agree well with long-lasting numerical simulations [48]. But we cannot draw definite conclusions about our model's inspiral performance because the results depend on the mass ratios, and extremely accurate, long-lasting NR simulations are not available, yet, for unequal masses. Therefore, we do not exclude other possible adjustments in the EOB model to keep track of the phase evolution for an extremely large number of GW cycles.

Using white noise and LIGO's PSD, we found FFs $\gtrsim$ 0.98, except for the $l = 4$, $m = 4$, $l = 3$, $m = 2$, and $l = 2$, $m = 1$ modes of mass ratio 4:1 (see Tables II and III). The matching procedure from inspiral(-plunge) to ringdown that we employ is too simplified when QNMs with different $l$ are present and/or the dominant frequency associated with the $l$, $m$ mode is rather different from the dominant frequency associated with the $l = 2$, $m = 2$ mode. This can show up as an earlier decoupling and higher QNM frequency (see the left panel of Fig. 8). We shall explore a more suitable matching procedure in the near future. In any case, when building the complete waveform containing all the relevant $l$, $m$ modes [see Eq. (43)] and takes into account their different amplitudes (see Fig. 8), we obtain rather high FFs, as seen in Table IV.

We pointed out, as already done in Ref. [9], that there exists a non-negligible difference in the amplitude of the PN (EOB or Taylor-expanded PN) and NR waveforms, whose origin has not yet been accounted for (see the right panel in Fig. 8). It might be due to higher-order PN corrections in the amplitude [7,11,43].

When maximizing over the binary masses, the p4PN-EOB template family presented here will have extremely high matching performances and can be used for coherent detection of nonspinning binary BHs, further improving the EOB model presented in Ref. [9]. Once the amplitude difference is resolved, the p4PN-EOB templates can be employed for parameter estimation for ground-based detectors. For LISA, which is expected to observe the coalescence of supermassive black holes with rather high signal-to-noise ratios, say $\sim 10^2$–$10^4$, the faithfulness to the model presented here is not high enough to allow accurate parameter estimation. Improvements to the EOB model, tuned to match the results of longer-lasting, and more highly accurate numerical simulations will be necessary. In this respect we notice that important advances have been made in solving numerically the two-body problem in the test-mass-limit case using Regge-Wheeler-Zerilli-type methods, and comparing it to the EOB model [12,13]. The authors of Refs. [12,13] introduced several improvements in the EOB approach. Notably, they include non-adiabatic quasicircular orbit terms, match the inspiral(-plunge) waveform to the ringdown modes over a time interval, instead of at one point, and include up to five ringdown overtones. These refinements lead to a reduction of the phase difference between the numerical and EOB waveforms from $\pm 3.5\%$ to $\pm 1.1\%$, and more importantly, to excellent agreement of the $l = 2$, $m = 2$ mode amplitude. Soon these improvements will be applied also in the comparable-mass case.

The results presented here point to the possibility that an essentially complete understanding of binary BH mergers, developed with the aid of highly accurate NR simulations, may be encoded in relatively simple, convenient analytic models for GW data analysis applications, avoiding the need for templates derived directly from NR simulation. In the future we plan to improve this analysis by including
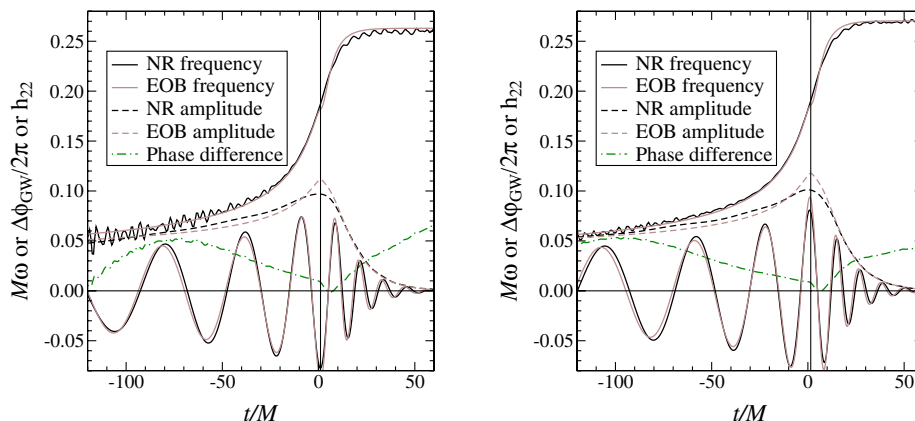


FIG. 9 (color online). In the left (right) panel we plot the NR and p4PN-EOB frequencies and amplitudes, and the phase difference between the p4PN-EOB and NR $h_{22}$ for a binary with mass ratio 2:1 (3:2). We maximize only over the initial phase and time of arrival.

higher-order PN amplitude corrections and to explore extensions of the model to spinning, precessing binary systems, using improved versions of the EOB model with spin [22,26].

## ACKNOWLEDGMENTS

## APPENDIX: COMPARISON WITH BINARIES OF MASS RATIO 2:1 AND 3:2

In Fig. 9 we show how the p4PN-EOB model performs for mass ratios 2:1 and 3:2. In these cases the waveforms are much shorter, and the eccentricity during the inspiral case is more pronounced. Details on these simulations can be found in Refs. [9,10].

[1] A. Abramovici *et al.*, Science **256**, 325 (1992); http://www.ligo.caltech.edu.

[2] B. Caron *et al.*, Classical Quantum Gravity **14**, 1461 (1997); http://www.virgo.infn.it.

[3] H. Lück *et al.*, Classical Quantum Gravity **14**, 1471 (1997); http://www.geo600.uni-hannover.de.

[4] M. Ando *et al.*, Phys. Rev. Lett. **86**, 3950 (2001); http://tamago.mtk.nao.ac.jp.

[5] http://www.lisa-science.org/resources/talks-articles/science/lisa_science_case.pdf.

[6] L. S. Finn, Phys. Rev. D **46**, 5236 (1992); L. S. Finn and D. F. Chernoff, Phys. Rev. D **47**, 2198 (1993).

[7] A. Buonanno, G. Cook, and F. Pretorius, Phys. Rev. D **75**, 124018 (2007).

[8] J. Baker, J. van Meter, S. McWilliams, J. Centrella, and B. J. Kelly, arXiv:gr-qc/0612024 [Phys. Rev. Lett. (to be published)].

[9] Y. Pan, A. Buonanno, J. G. Baker, J. Centrella, B. J. Kelly, S. T. McWilliams, F. Pretorius, and J. R. van Meter, arXiv:gr-qc/07041964 [Phys. Rev. D (to be published)].

[10] J. Schnittman, A. Buonanno, J. R. van Meter, J. G. Baker, W. D. Boggs, J. Centrella, B. J. Kelly, and S. T. McWilliams (unpublished).

[11] M. Hannam, S. Husa, U. Sperhake, B. Brügmann, and J. A. Gonzalez, arXiv:0706.1305.

[12] A. Nagar, T. Damour, and A. Tartaglia, Classical Quantum Gravity **24**, S109 (2007); T. Damour and A. Nagar, in *Proceedings of XIth Marcel Grossmann Meeting, Berlin, 2006*, edited by H. Kleinert, R. T. Jantzen, and R. Ruffini (World Scientific, Singapore, 2007).

[13] T. Damour and A. Nagar, Phys. Rev. D **76**, 064028 (2007).

[14] See, e.g., L. Blanchet, Living Rev. Relativity **5**, 3 (2002), http://www.livingreviews.org/lrr-2002-3.

[15] P. Jaranowski and G. Schäfer, Phys. Rev. D **57**, 7274 (1998); **63**, 029902 (2000).

[16] T. Damour, P. Jaranowski, and G. Schäfer, Phys. Lett. B **513**, 147 (2001).

[17] T. Damour, P. Jaranowski, and G. Schäfer, Phys. Rev. D **62**, 021501 (2000); **63**, 029903 (2000).

[18] L. Blanchet and G. Faye, Phys. Rev. D **63**, 062005 (2001); V. C. de Andrade, L. Blanchet, and G. Faye, Classical Quantum Gravity **18**, 753 (2001); L. Blanchet, G. Faye, B. R. Iyer, and B. Joguet, Phys. Rev. D **65**, 061501 (2002); **71**, 129902 (2005); L. Blanchet and B. R. Iyer, Classical Quantum Gravity **20**, 755 (2003); L. Blanchet, T. Damour, G. Esposito-Farese, and B. R. Iyer, Phys. Rev. Lett. **93**, 091101 (2004).

[19] L. Kidder, C. Will, and A. Wiseman, Phys. Rev. D **47**, R4183 (1993); L. Kidder, Phys. Rev. D **52**, 821 (1995); B. Owen, H. Tagoshi, and A. Ohashi, Phys. Rev. D **57**, 6168 (1998); H. Tagoshi, A. Ohashi, and B. Owen, Phys. Rev. D **63**, 044006 (2001); L. Blanchet, A. Buonanno, and G. Faye, Phys. Rev. D **74**, 104034 (2006); G. Faye, L. Blanchet, and A. Buonanno, Phys. Rev. D **74**, 104033 (2006).

[20] A. Buonanno and T. Damour, Phys. Rev. D **59**, 084006 (1999).

[21] T. Damour, P. Jaranowski, and G. Schäfer, Phys. Rev. D **62**, 084011 (2000).

[22] T. Damour, Phys. Rev. D **64**, 124013 (2001).

[23] A. Buonanno and T. Damour, Phys. Rev. D **62**, 064015 (2000).

[24] T. Damour and A. Nagar, Phys. Rev. D **76**, 044003 (2007).

[25] A. Buonanno and T. Damour, in *Proceedings of IXth Marcel Grossmann Meeting, Rome, 2000*, edited by V. G. Gurzadyan, R. T. Jantzen, and R. Ruffini (World Scientific, Singapore, 2002).

[26] A. Buonanno, Y. Chen, and T. Damour, Phys. Rev. D **74**, 104005 (2006).

[27] T. Damour, B. R. Iyer, and B. S. Sathyaprakash, Phys. Rev. D **57**, 885 (1998).

[28] F. Pretorius, Phys. Rev. Lett. **95**, 121101 (2005); M. Campanelli, C. O. Lousto, P. Marronetti, and Y. Zlochower, Phys. Rev. Lett. **96**, 111101 (2006); J. Baker, J. Centrella, D. Choi, M. Koppitz, and J. van Meter, Phys. Rev. Lett. **96**, 111102 (2006).

[29] M. Campanelli, C. O. Lousto, and Y. Zlochower, Phys. Rev. D **74**, 041501 (2006); **74**, 084023 (2006); U.

Sperhake, arXiv:gr-qc/0606079 [Phys. Rev. D (to be published)]; J. González, U. Sperhake, B. Brügmann, M. Hannam, and S. Husa, Phys. Rev. Lett. **98,** 091101 (2007); B. Szilagyi, D. Pollney, L. Rezzolla, J. Thornburg, and J. Winicour, Classical Quantum Gravity **24,** S275 (2007); F. Pretorius and D. Khurana, Classical Quantum Gravity **24,** S83 (2007); B. Vaishnav *et al.*, Phys. Rev. D **76,** 084020 (2007).

[30] T. Damour, E. Gourgoulhon, and P. Grandclément, Phys. Rev. D **66,** 024007 (2002).

[31] T. Damour, B. Iyer, P. Jaranowski, and B. Sathyaprakash, Phys. Rev. D **67,** 064028 (2003).

[32] E. Brézin, C. Itzykson, and J. Zinn-Justin, Phys. Rev. D **1,** 2349 (1970).

[33] A. Buonanno, Y. Chen, and M. Vallisneri, Phys. Rev. D **67,** 024016 (2003); **74,** 029903(E) (2006).

[34] T. Damour and A. Gopakumar, Phys. Rev. D **73,** 124006 (2006).

[35] C. V. Vishveshwara, Nature (London) **227,** 936 (1970); B. Schutz and C. M. Will, Astrophys. J. **291,** L33 (1985); S. Chandrasekhar and S. Detweiler, Proc. R. Soc. A **344,** 441 (1975).

[36] W. Press, Astrophys. J. **170,** L105 (1971).

[37] M. Davis, R. Ruffini, W. H. Press, and R. H. Price, Phys. Rev. Lett. **27,** 1466 (1971); M. Davis, R. Ruffini, and J. Tiomno, Phys. Rev. D **5,** 2932 (1972).

[38] R. H. Price and J. Pullin, Phys. Rev. Lett. **72,** 3297 (1994); R. J. Gleiser, C. O. Nicasio, R. Price, and J. Pullin, Classical Quantum Gravity **13,** L117 (1996); Phys. Rev. Lett. **77,** 4483 (1996); P. Anninos, D. Hobill, E. Seidel, L. Smarr, and W. M. Suen, Phys. Rev. Lett. **71,** 2851 (1993); J. G. Baker, A. Abrahams, P. Anninos, S. Brandt, R. Price,

J. Pullin, and E. Seidel, Phys. Rev. D **55,** 829 (1997); Z. Andrade and R. H. Price, Phys. Rev. D **56,** 6336 (1997).

[39] E. Gourgoulhon, P. Grandclément, and S. Bonazzola, Phys. Rev. D **65,** 044020 (2002); P. Grandclément, E. Gourgoulhon, and S. Bonazzola, Phys. Rev. D **65,** 044021 (2002).

[40] L. Blanchet, Phys. Rev. D **65,** 124009 (2002).

[41] G. B. Cook and H. P. Pfeiffer, Phys. Rev. D **70,** 104016 (2004); M. Caudill, G. B. Cook, J. D. Grigsby, and H. Pfeiffer, Phys. Rev. D **74,** 064011 (2006).

[42] Y. Wiaux, L. Jacques, and P. Vandergheynst, arXiv:astro-ph/0508514.

[43] J. Baker, S. McWilliams, J. van Meter, J. Centrella, D. Choi, B. J. Kelly, and M. Koppitz, Phys. Rev. D **75,** 124024 (2007).

[44] J. Baker, M. Campanelli, and C. Lousto, Phys. Rev. D **65,** 044001 (2002).

[45] E. W. Leaver, Proc. R. Soc. A **402,** 285 (1985); F. Echeverria, Phys. Rev. D **40,** 3194 (1989); E. Berti, V. Cardoso, and C. Will, Phys. Rev. D **73,** 064030 (2006).

[46] E. Berti, V. Cardoso, J. A. Gonzalez, U. Sperhake, M. Hannam, S. Husa, and Bernd Brügmann, Phys. Rev. D **76,** 064034 (2007).

[47] See J. González *et al.* (Ref. [29]).

[48] M. Boyle *et al.* (Caltech/Cornell collaboration), http://baba.astro.cornell.edu/~ecgm10/Proceedings/mroue.pdf.

[49] T. Damour, B. Iyer, and B. Sathyaprakash, Phys. Rev. D **63,** 044023 (2001); **66,** 027502 (2002); **67,** 064028 (2003).

[50] L. Blanchet, B. R. Iyer, C. M. Will, and A. G. Wiseman, Classical Quantum Gravity **13,** 575 (1996).